



Gradient wick channels for enhanced flow boiling HTC and delayed CHF

Masoud Ahmadi, Sajjad Bigham*

Department of Mechanical Engineering-Engineering Mechanics, Michigan Technological University, 1400 Townsend Drive, Houghton, USA



ARTICLE INFO

Article history:

Received 23 February 2020

Revised 23 November 2020

Accepted 25 November 2020

Available online 17 December 2020

Keywords:

Flow boiling

Gradient wick channels

Capillary limit

Textured surfaces

3D wick structure

ABSTRACT

Liquid supply to wick structures of flow boiling surfaces is fundamentally restricted by the capillary limit at which the pressure drop of the wicked liquid surpasses texture-amplified capillary forces. Gradient wick structures partially decouple permeability and capillary pressure, thereby delaying the capillary limit. In this study, gradient wick channels facilitating out-of-plane liquid delivery are introduced to postpone the capillary limit and thus enhance the two-phase flow boiling heat transfer coefficient (HTC) and delay critical heat flux (CHF). Here, the permeability of the gradient wick channels is augmented by large-pore-size meshes employed near the bulk fluid while capillary pressure is maximized by small-pore-size meshes utilized near the hot boiling surface. This combination of wick structures enables to preferentially guide the cooling liquid, deionized water, from the far-field cold liquid toward the bottom hot substrate. The spatial distribution of individual gradient wick channels promotes separate liquid-vapor pathways, thus facilitating the vapor escape process. Experiments conducted here reveal that the flow boiling performance metrics of the proposed heat sink leveraging the gradient wick channels outperform those of the homogenous wick channels and solid fin channels. The proposed heat sink demonstrates a strong liquid mass flux dependency due to a combination of convective boiling and amplified wickability effects. The enhanced convective boiling could be related to surface roughness, a high number of active nucleation sites, and a large surface area available through tortuous passages of wick channels. At higher mass flow rates, effective capillary pressure available for out-of-plane wicking action also increases, thereby further boosting the wickability effect and associated heat transfer processes. This could meaningfully delay the CHF. In fact, the CHF limit was not observed on the gradient wick channel surfaces in the mass flux and wall superheat range studied. The experimental results indicated a maximum heat flux of 870 W/cm² with a gradient wick channel heat sink, a 60% improvement compared with a plain copper surface. Furthermore, a maximum HTC of 1000 kW/m²-K at a wall superheat of 3 °C was observed, a three-fold enhancement compared with that of the plain surface. The proposed gradient wick channel topology offers new pathways for designing innovative surface technologies with high heat removal capabilities, thereby potentially improving the energy economy in myriad modern energy applications.

© 2020 Elsevier Ltd. All rights reserved.

1. Introduction

For more than a century, thermal management has played a key role in the advancement of various technological and industrial applications such as power generation, refrigeration, desalination, and high-power electronics. The microelectronic industry, in particular, relies on improvements in micro-scale thermal management techniques to continue its current performance growth trajectory. Among many thermal management pathways, liquid-to-vapor phase change cooling has been recognized as a promising solution for high heat flux applications [1–4]. By taking advan-

tage of latent heat of vaporization, the evaporative phase change cooling can dissipate high heat fluxes with a small streamwise temperature change while reducing the required liquid flow rate and pumping power [5,6]. Over the last half-century, numerous attempts have been made to improve the efficiency of the phase-change heat transfer process in extremely demanding applications such as fusion reactor blankets [7,8] as well as many military electronic systems [9,10]. Despite remarkable progress, existing thermal management techniques and their architectural designs need to be revolutionized to address the ever-increasing cooling demands of next-generation high-heat-flux devices.

A majority of phase-change cooling solutions explored in the past rely on various surface modification techniques to enhance HTC and/or delay the CHF limit. This ranges from utilization of

* Corresponding author.

E-mail address: sbigham@mtu.edu (S. Bigham).

additional nucleation sites [11–14], enhanced wettability, wickability, and/or area by micro-nano structures/nanowires/porous media [15–24] to deposition of graphene oxide [25–27]. An important common functionality offered by many of these textured surfaces is wickability generally appearing when a dry spot is present. The dry spot could be either a transient local phenomenon created by individual growing bubbles especially during the early stages of the boiling process and/or a semi-sustained large dry pocket particularly the ones formed in the vicinity of the CHF limit [28–30].

Many of the textured surfaces preferentially stimulate in-plane liquid delivery to dry spots where liquid paths rewetting the surface are parallel to the bottom hot substrate. Chu et al. [20,21], for instance, fabricated microstructures with different geometries to experimentally investigate surface roughness-augmented wickability on CHF during pool boiling. They hypothesized that increasing the surface roughness increases surface forces at the liquid/vapor interface of each bubble (i.e., in-plane liquid delivery to a local dry spot) and thus delaying the CHF. An enhancement in CHF of approximately 160% was demonstrated on the roughest surface tested. More recent studies considered surface wettability/wickability as the main parameter affecting CHF and HTC in two-phase heat sinks and attempted to improve heat transfer characteristics through the utilization of in-plane wick structures. Forrest et al. [31], for example, studied pool boiling characteristics of polymer/SiO₂ nanoparticles applied to nickel wire using a layer-by-layer (LbL) deposition method and demonstrated up to 100% enhancement in the CHF limit. The drastic change in surface wettability caused by the LbL deposition method was identified as the major parameter affecting the CHF limit. Similarly, Yang et al. [17] utilized hydrophilic silicon nanowires to enhance the CHF value by merging all flow boiling regimes into a single one. It was demonstrated that the tailored nanostructures dominate surface tension force resulting in the formation of a single annular flow regime during flow boiling in microchannels. Heat fluxes up to approximately 400 W/cm² were removed from the surface using this approach.

A more fundamental study on the effect of wickability on critical heat flux was conducted by Rahman et al. [32]. They investigated the boiling process on surfaces with micro, nano, and hierarchical structures, and observed linear relation between CHF and in-plane wickability of structures employed. They also showed that, although decreasing the contact angle can increase CHF, wickability plays the main role in increasing the CHF limit at contact angles equal to zero (i.e., superhydrophilic nano-structured surfaces). A hierarchical fabricated surface showed to enhance CHF value up to 260 W/cm² with water under atmospheric conditions.

In contrast to the in-plane liquid delivery to dry-spots, some other engineered surfaces such as modulated porous-layer coatings [33], separate vapor-liquid pathways through bubble-induced macro-convection [34], nanostructured bi-conductive biphilic surfaces [35,36], and gradient wick structures with micro-chimney effect [37] favorably promote out-of-plane liquid delivery decoupling replenishing liquid from the vapor escape paths. Liter and Kaviany [33], for instance, showed that through the utilization of modulated (periodically non-uniform thickness) porous-layer coatings, liquid and vapor phases can be separated to reduce liquid-vapor counter flow resistance adjacent to the surface. Two different limits (hydrodynamic limit and viscous drag limit) were introduced as possible liquid-choking restrictions. It was shown that the measured CHF experienced by the coated surface is governed by the lower of the two limits. In this approach, the pool boiling CHF was enhanced nearly three times over that of a plain surface.

The out-of-plane liquid delivery approach also helps the separation of vapor and liquid pathways, thereby further delaying the CHF limit. Kandlikar et al. [38,39] promoted this idea through the implementation of tapered manifolds on top of a microchannel

heat sink. The excess volume provided by the manifold would allow the liquid flow to push the generated bubbles away from the surface and delay the CHF limit. The CHF values achieved in this approach were noticeably higher (CHF ~ 700 W/cm²) compared to the previous values reported in the literature (~ 100-300 W/cm²) and attested to the importance of efficient bubble removal on increasing CHF. More recently, researchers have pursued a novel perspective to push the CHF limit in the boiling process by incorporating low-conductivity materials at the liquid-solid interface. Rahman et al. [35] showed that a more than 5-fold enhancement in heat transfer rate can be achieved if approximately 18% of the boiling surface is replaced by a non-conductive epoxy. Low thermal conductivity regions promote liquid delivery toward the boiling surface by suppressing bubble nucleation. High-temperature high thermal conductivity areas facilitate bubble formation, growth, and departure processes, and thereby separating liquid and vapor pathways.

David et al. [40] first proposed a new concept for two-phase vapor venting microchannel heat sinks utilizing PTFE membranes to extract vapor bubbles into separate vapor transport channels. A maximum CHF of ~80 W/cm² was achieved while the normalized pressure drop was reduced by almost 60%. They concluded that the main advantage of a venting device over a non-venting heat sink can be recognized in devices with very small liquid channels as it maximizes heat transfer coefficients and improves flow stability. In an alternative strategy, Fazeli et al. [41,42] introduced a novel architecture for two-phase heat sinks in which cooling liquid is pumped to engineered evaporating menisci. A porous hydrophobic membrane directly bonded on top of the microscale heat sink separated liquid and vapor phases inside the device. Having no liquid flow discharge (i.e., only vapor exits through the porous polymeric membrane), the implemented flow arrangement enabled subjecting bubbles to omnidirectional pressure, thereby limiting their surface coverage. Furthermore, bubble extraction could be improved simply by raising the liquid pressure inside the device, which leads to higher CHF values.

Utilizing a unique approach, Palko et al. [16] demonstrated high heat fluxes in an innovative two-phase heat sink utilizing laser micromachined diamond heat spreaders and copper mesh phase separators. The diamond heat spreaders enhanced the overall heat transfer area by a factor of 3, while phase separation structures controlled liquid-vapor flow distribution. A maximum heat flux removal rate of ~1300 W/cm² was reported at a full device scale (0.7 cm²).

Here, we utilize novel gradient wick channels to delay the capillary limit and facilitate out-of-plane liquid delivery for enhanced flow boiling HTC and delayed CHF limit. In the following sections, first, the new gradient wick channel concept is explained. Then, the experimental test facility and its accuracy are introduced. Finally, observed flow boiling regimes and measured thermal performance values are discussed at different thermo-hydraulic conditions.

2. Concept

In the competition between a cooling liquid and its vapor trying to occupy a hot solid surface, the vapor phase appears to temporarily displace the cooling liquid near the CHF limit. This leads to the formation of an unstable low-thermal-conductivity vapor film that significantly deteriorates the heat transfer rate. To delay the CHF limit, micro and nano-textured surfaces representing homogenous wick structures are typically utilized [20,21,32,36,43,44] to augment liquid wickability by texture-amplified capillary forces. Prior studies indeed confirmed that surface structures can enhance CHF limit by up to 160%, and 53.3% in the pool [21], and flow boiling [43] processes, respectively. Additionally, it has been lately shown

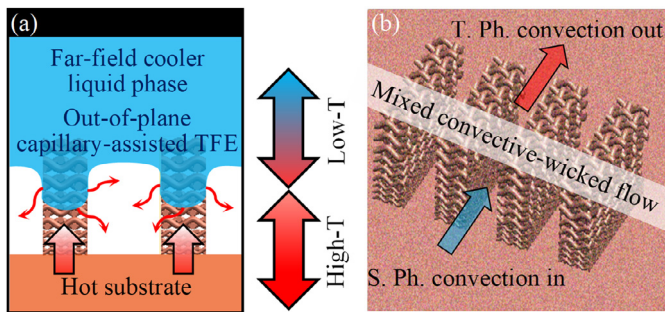


Fig. 1. (a) A schematic of a possible liquid-vapor interface for the gradient wick channels, and (b) a 3D schematic of the gradient wick channel heat sink. T.F.E., S.Ph. and T.Ph. stand for thin film evaporation, single-phase, and two-phase, respectively.

that there is an optimal texture density at which CHF value maximizes in both pool boiling [44] and flow boiling [43] processes. The thermal performances of these in-plane homogenous wick structures, however, are primarily limited by the capillary limit. At the capillary limit, capillary forces generated by a wick structure are balanced by the sum of pressure drops associated with the liquid flow wicked into the structures. Homogenous wick structures employing small pore sizes exhibit high capillary pressures but low permeability. On the other hand, homogenous wick structures utilizing large pore sizes demonstrate high permeability but low capillary pressures. Hybrid and gradient wick structures with an engineered large and small pore size distribution could partially decouple permeability and capillary pressure, thereby delaying the capillary limit.

In this study, gradient wick channels utilizing an innovative thermo-fluidic design topology are introduced to enhance the two-phase flow boiling heat transfer coefficient (HTC) and delay critical heat flux (CHF). As shown in Fig. 1, the permeability of the gradient wick channels is improved by large-pore-size copper meshes employed near the bulk fluid while the capillary pressure is maximized by small-pore-size meshes utilized near the hot boiling surface. A medium-pore-size mesh is utilized in the middle. This combination of wick structures facilitates out-of-plane capillary-assisted liquid delivery in which the cooling liquid is preferentially guided from the far-field cold liquid toward the bottom hot substrate. Here, flow boiling performance is improved due to the presence of a highly-efficient thin film evaporation heat transfer mechanism at the sidewalls and within the gradient wick channels (cf. Fig. 1). In the proposed boiling surface, height has a critical role as it functions as a thermal-wick bridge between the cooler far-field liquid phase and the bottom hot substrate. The liquid wicked into the bridge may or may not reach the bottom substrate depending on local heat flux (i.e., evaporation rate within a wick channel) and micro-inflow liquid wicking rate at the capillary limit. Moreover, the proposed wick channels support separate liquid and vapor pathways for the enhanced heat transfer process.

3. Experiment

3.1. Fabrication procedure and characteristics of heat sinks

Woven copper meshes with fine, medium, and coarse pore size characteristics (cf. Table 1) were diffusion bonded to fabricate heat sinks employing gradient wick channels as shown in Fig. 2. First, the copper mesh layers and the support 6-mm-thick copper substrate were cleaned with acetone, isopropyl alcohol, and de-ionized (DI) water. Then, the meshes and the copper substrate were mechanically sandwiched. The sandwiched assembly was then placed in a custom-made vacuum chamber and subsequently heated to a high-temperature level of about 700 °C. The chamber pressure is

monitored by a pressure transducer and controlled with a vacuum pump to prevent oxidation at high temperatures. For a successful diffusion bonding process, the assembly was kept at high temperatures for a minimum of four hours. The result was a mechanically robust diffusion bonded assembly. The diffusion bonded assembly was then machined in a 1 cm² area with a high precision micro-CNC tool to create individual channel topologies. Two heat sinks employing gradient wick channels with heights of 2.5 mm (referred to GW2.5) and 4.2 mm (referred to GW4) were fabricated to investigate the effect of the gradient wick structure on flow boiling HTC and CHF limit. Fig. 2 shows details and scanning electron microscope (SEM) images of a fabricated gradient wick channel heat sink. Three additional heat sinks utilizing homogenous wick channels with medium pore size meshes and a height of 4 mm (referred to HW4-medium), solid fin channels with a height of 4 mm (referred to SF4), and a plain copper substrate (referred to P0) were also fabricated for comparison. Dimensional characteristics and the number of metallic copper mesh layers employed for gradient and homogenous wick channel heat sinks are presented in Table 1. Geometrical details of different heat sinks examined are also described in Table 2.

3.2. Permeability measurement test setup and procedure

A custom-made permeability test setup shown in Fig. 3 was employed to characterize and compare the permeability of the homogenous and gradient wick structures of the proposed study. The wick structures were sandwiched between two stainless steel plates and then placed in a closed water flow loop. The working fluid, DI water, was pumped through the wick test section with a submerged pump. A differential pressure transducer (Model: Omega-PX26-005DV) measured the pressure difference between the inlet and outlet of the test section at different mass flow rates. The mass flow rate of the fluid was measured with a variable area flow meter (Model: Omega-FT044-15-ST-VN). Three homogeneous wick structures consisting of either small (i.e., 228.6 μm), medium (i.e., 279.4 μm), or coarse (i.e., 381 μm) pore size meshes were considered. The gradient wick structure comprised of all three small, medium, and coarse pore size meshes each at an equal thickness of about 1.33 mm. The overall thickness of the three homogenous and the gradient wick structures was 4 mm. The overall wick thickness represents the flow length of the wick structure.

Darcy's law formulates the flow of a fluid through a wick structure. Darcy's law defines the permeability parameter κ as the ability of the wick media to pass the flow through.

$$\kappa = \frac{\dot{m}\mu l}{\rho A \Delta P} \quad (1)$$

where κ is permeability [m²], \dot{m} is mass flow rate [kg/s], μ is working fluid dynamic viscosity [Pa.s], l is wick thickness [m], ρ is fluid density [kg/m³], A is flow surface area of the wick [m²], and ΔP is pressure difference between the two sides of the wick [Pa].

Experiments were conducted to measure the flow pressure drop through the wick structures at different mass flow rates. The permeability of each wick structure was then calculated by the slope of $\dot{m}\mu l$ versus $\rho A \Delta P$ curve. A linear fit was passed through individual experimental data points of each wick structure to calculate the slope of the curve and thus the permeability.

3.3. Flow boiling test facility and procedure

Fig. 4a shows an image of a heat sink with four parallel wick channels. The heat sinks were enclosed with a top stainless steel cap including inlet and outlet manifolds as shown in Fig. 4b. Fig. 4c shows the flow boiling test setup facility. The copper substrate was

Table 1
Copper mesh characteristics employed for gradient and homogenous wick channel heat sinks.

Mesh type	Number of wires per square inch	Wire diameter (μm)	Pore size [μm]	Number of bonded copper mesh layers for		
				GW2.5	HW4-med.	GW4
Fine	60 × 60	190	228.6	4	0	8
Medium	50 × 50	230	279.4	3	21	7
Coarse	40 × 40	254	381	3	0	6

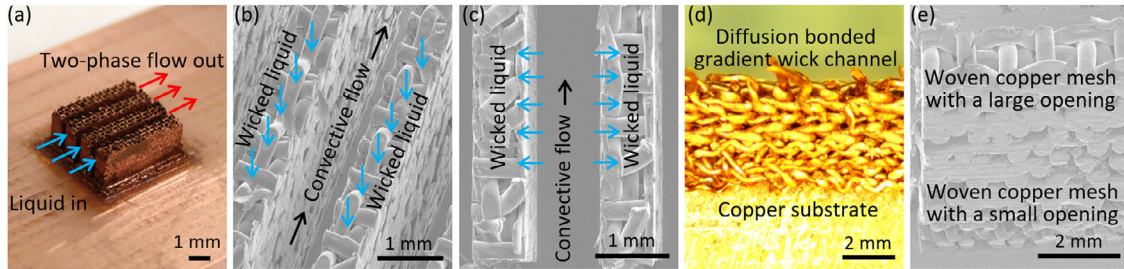


Fig. 2. (a) An image of a fabricated heat sink with gradient wick channels, (b) an isometric-view SEM image, (c) a top-view SEM image, (d) a cross-sectional view, and (e) a side-view SEM of a gradient wick channel.

Table 2
Different heat sinks examined and their geometrical characteristics.

Heat sink	Type	Channel height [mm]	Flow width [μm]	Wick/solid width [μm]
P0	Plain copper substrate	N/A	N/A	N/A
GW2.5	Gradient wick channels	2.5	940	690
SF4	Solid fin channels	4	940	690
HW4-med.	Homogenous wick channels	4	940	690
GW4	Gradient wick channels	4.2	940	690

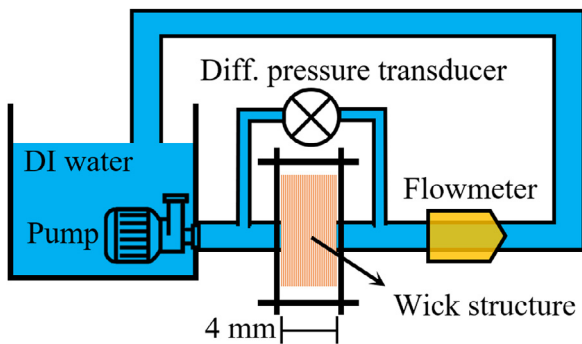


Fig. 3. A schematic of the permeability test setup.

equipped with three embedded T-type thermocouples which were placed just below the parallel wick channels with an overall boiling surface area of 1 cm^2 (cf. Fig. 4a). Three 1.5-kW cartridge heaters hosted in a heating block were utilized to heat the test section. The heating block and the test section were connected by a one-dimensional heat transfer column with a cross-sectional surface area of 1 cm^2 . A 1-mm-in-depth pocket with a footprint surface area of 1 cm^2 was machined on the back of the copper substrates

to ensure heat was provided exactly to the effective boiling surface area. A thermal paste was applied between the copper substrate and the heating block to reduce interfacial thermal resistances. The test section and the heating block assembly were well insulated using mineral wool. An adhesive Kapton film and a rubber sheet were utilized to enclose the boiling heat transfer area to the wick channels with a projected footprint area of 1 cm^2 . The adhesive Kapton film remained intact after the boiling experiments. A fixed distance of 1.8 mm was used between the top of wick channels and the bottom of the cap in all boiling experiments (cf. Fig. 4b). A differential pressure transducer (Model: Omega-PX26-005DV) was used to measure the pressure drop across the test section. Temperature and pressure variations were recorded by a high accuracy data acquisition system (Model: Agilent 34970A).

Dry tests and test setup heat loss: To measure thermal heat losses of the flow boiling test setup to the surrounding ambient environment, dry tests at different heating block temperatures were conducted. Here, the thermal energy required to keep the heating block at a fixed temperature was considered as the test setup heat loss. A sample dummy heat sink was used during the dry test. No fluid was passed through the dummy heat sink. The tests were conducted at a heating block temperature range observed during the actual flow boiling experiments. Fig. 5 shows

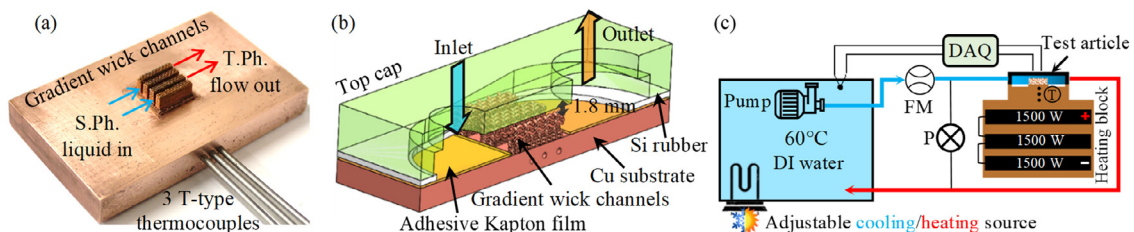


Fig. 4. (a) An image of the test article with embedded thermocouples, (b) a schematic of the test article, and (c) a schematic of the flow boiling test facility.

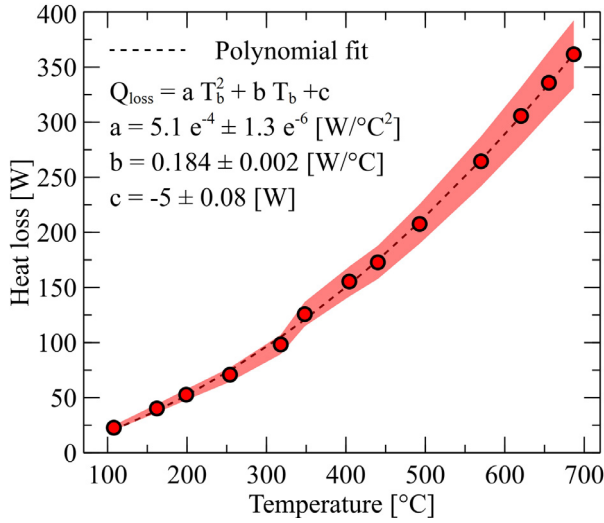


Fig. 5. Heat loss of the flow boiling test setup at different heating block temperatures.

heat loss of the flow boiling test setup at different heating block temperatures. The heat losses at different block temperatures were calculated by measuring input voltages and corresponding currents to the cartridge heaters. A polynomial function was fitted to data and used to calculate setup heat loss at different block temperatures during actual flow boiling experiments.

Flow boiling test procedure: The working fluid was first degassed by vigorous boiling before each flow boiling test. During the flow boiling experiments, the working fluid, deionized water, was pumped to the test section from a constant temperature reservoir kept at approximately 60 °C. The temperature of the supply liquid reservoir was controlled by a submerged heat exchanger with cooling and heating capabilities. For each experimental data point, the power provided to the heating block was maintained constant. Then, each flow boiling test point was allowed at least 40 min to reach a semi-steady state condition at which there was no continuous rise and/or decline in each temperature reading. Once a semi-steady state was assured, the net thermal energy provided to the heat sink was calculated by measuring the total power input provided to the test setup minus the setup heat loss at the established block temperature.

Repeatability and aging effect: Each experimental test condition was repeated at least four times ensuring repeatability of the reported data points. The flow boiling surfaces were carefully cleaned by a “chemical polishing” method [45] to bring consistency to the test surfaces before each round of flow boiling tests. First, the heat sink was immersed in a 15% weight percent nitric acid for 15 min and a consistent stirring level. It was then cleaned with DI water and dried on a hot plate at 60 °C for 10 min. The test results of a fresh flow boiling surface (i.e., a newly fabricated flow boiling surface) was always different and higher than subsequent test results associated with aged flow boiling surfaces. Fig. 6 shows surface heat flux as a function of wall superheat for a fresh and an aged GW4 wick structure. As evident, the thermal performance of the fresh flow boiling surface was significantly higher than the aged GW4 flow boiling surface. This could be attributed to nucleation sites’ size distribution and water wettability, which might differ between a fresh and an aged copper surface. Once a heat sink surface reached high-temperature values in the first flow boiling test, an oxide layer appeared on the copper surface changing its boiling behavior particularly in the nucleate boiling regime where solid surface properties (i.e., nucleation sites’ size distribution and wettability) are highly important. The flow boiling test

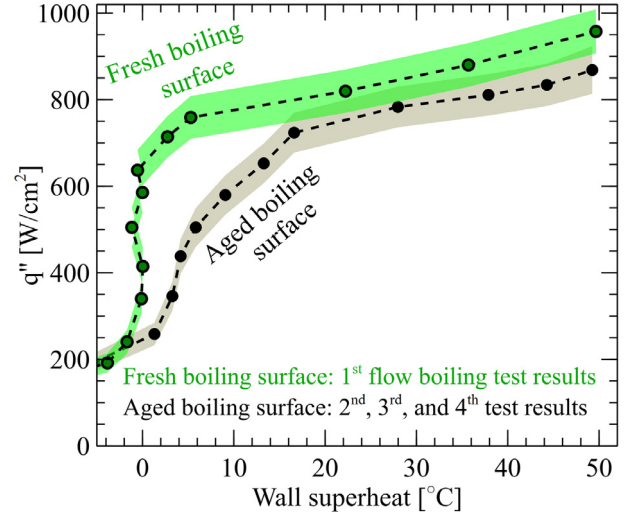


Fig. 6. Flow boiling performance of a fresh and an aged GW4 wick structure.

results showed a consistent thermal behavior on cleaned (as described above) aged copper surfaces with an almost similar boiling behavior in the second, third, and fourth flow boiling experiments. The flow boiling test results reported in this study all represent performances of cleaned aged copper surfaces.

3.4. Data reduction and uncertainty analysis

The net thermal energy dissipated during the phase change process (Q_{net}) is calculated by subtracting the heat loss (Q_{loss}) at a given heating block temperature from the total energy applied to the heat sink (Q_{total}) as follows:

$$Q_{net} = Q_{total} - Q_{loss} \quad (2)$$

The uncertainty associated with the total energy supplied ($Q_{total} = V \times I$) is calculated as follows:

$$\frac{\delta Q_{total}}{Q_{total}} = \sqrt{\left(\frac{\delta V}{V}\right)^2 + \left(\frac{\delta I}{I}\right)^2} \quad (3)$$

where V and I are supplied voltage and current to the cartridge heaters. The setup heat loss, Q_{loss} , was calculated from the polynomial fit derived from the dry tests as $Q_{loss} = aT_b^2 + bT_b + c$ where T_b is the heating block temperature. The uncertainty associated with heat loss can be calculated as follows:

$$\delta Q_{loss} = \sqrt{(\delta(aT_b^2))^2 + (\delta(bT_b))^2 + (\delta c)^2} \quad (4)$$

where

$$\frac{\delta(aT_b^2)}{aT_b^2} = \sqrt{\left(\frac{\delta a}{a}\right)^2 + \left(2\frac{\delta T_b}{T_b}\right)^2} \quad (5)$$

$$\frac{\delta(bT_b)}{bT_b} = \sqrt{\left(\frac{\delta b}{b}\right)^2 + \left(\frac{\delta T_b}{T_b}\right)^2} \quad (6)$$

Therefore, the uncertainty associated with the net heat dissipation can be estimated as:

$$\delta Q_{net} = \sqrt{(\delta Q_{total})^2 + (\delta Q_{loss})^2} \quad (7)$$

The dissipated heat flux (q'') from a heat sink device can be then calculated by dividing the net heat dissipation into the projected heat sink area (i.e., $A_{proj} = 1 \text{ cm}^2$) as follows:

$$q'' = \frac{Q_{net}}{A_{proj}} \quad (8)$$

The uncertainty associated with the heat flux can be estimated as follows:

$$\frac{\delta q''}{q''} = \sqrt{\left(\frac{\delta Q_{net}}{Q_{net}}\right)^2 + \left(\frac{\delta A_{proj}}{A_{proj}}\right)^2} \quad (9)$$

The heat transfer coefficient is evaluated from Newton's law of cooling as follows:

$$h = \frac{q''}{(T_s - T_{sat})} \quad (10)$$

where T_s and T_{sat} are the surface temperature at the solid-liquid interface and the saturation temperature of the working fluid, respectively. The surface temperature is estimated from Fourier's law of heat conduction equation considering the net heat flux as follows:

$$T_s = T_{ave} - \frac{\Delta x}{k_c} q'' \quad (11)$$

where T_{ave} is the average temperature of the three embedded thermocouples in the copper substrate, Δx is the vertical distance between the center of the thermocouple holes to the solid-liquid interface, and k_c is the copper thermal conductivity. The uncertainty associated with the surface temperature can be estimated as:

$$\delta T_s = \sqrt{(\delta T_{ave})^2 + (\delta(\Delta x q''/k_c))^2} \quad (12)$$

where

$$\delta T_{ave} = \sqrt{(\delta T_1)^2 + (\delta T_2)^2 + (\delta T_3)^2} \quad (13)$$

$$\delta\left(\frac{\Delta x}{k_c} q''\right) = \left(\frac{\Delta x}{k_c} q''\right) \sqrt{\left(\frac{\delta q''}{q''}\right)^2 + \left(\frac{\delta \Delta x}{\Delta x}\right)^2} \quad (14)$$

where T_1, T_2 and T_3 are the three embedded thermocouples in the copper substrates.

The saturation temperature of the working fluid is a function of the fluid pressure within the heat sink (hereafter referred to as far-field average pressure) as follows:

$$T_{sat} = T_{sat,water}(P_{far-field\ ave.}) \quad (15)$$

The fluid pressure varies along the channel and thus its saturation temperature. The fluid far-field average pressure is the average of the fluid inlet and outlet pressure values as follows:

$$P_{far-field\ ave.} = \frac{P_{out} + P_{in}}{2} \quad (16)$$

where P_{out} is the outlet fluid pressure and assumed the atmospheric pressure (i.e., 103-106 kPa depending on test date). Utilizing a second pressure transducer verified that the outlet fluid is the atmospheric pressure as the outlet fluid was immediately discharged with a large tube diameter to a reservoir maintained at the atmospheric pressure. Also, P_{in} is the fluid inlet pressure and calculated from the differential pressure transducer. The flow boiling curves are plotted against the wall superheat defined as the difference between the surface temperature (i.e., Eq. 11) and the saturation temperature of the working fluid (i.e., Eq. 15).

Hence, the uncertainties associated with the heat transfer coefficient can be calculated as follows:

$$\frac{\delta h}{h} = \sqrt{\left(\frac{\delta q''}{q''}\right)^2 + \left(\frac{\delta(T_s - T_{sat})}{T_s - T_{sat}}\right)^2} \quad (17)$$

where

$$\delta(T_s - T_{sat}) = \sqrt{(\delta T_s)^2 + (\delta T_{sat})^2} \quad (18)$$

Additionally, the uncertainty associated with the permeability is calculated as follows:

$$\frac{\delta \kappa}{\kappa} = \sqrt{\left(\frac{\delta \dot{m}}{\dot{m}}\right)^2 + \left(\frac{\delta l}{l}\right)^2 + \left(\frac{\delta A}{A}\right)^2 + \left(\frac{\delta \Delta P}{\Delta P}\right)^2} \quad (19)$$

Furthermore, the void cross-sectional area available for the fluid flow (i.e., open area between and above the wick channels) was considered to calculate the mass flux. Table 3 shows the range and uncertainty of the main parameters.

4. Results and discussion

4.1. Permeability of homogenous and gradient wick structures

Permeability of homogenous and gradient wick structures was characterized to understand the role of gradient topology in the capillary limit. Three homogenous wick structures with coarse (HW4-coarse), medium (HW4-medium), and fine (HW4-fine) pore size meshes and a gradient wick structure (GW4) were studied. The thickness of all wick structures was 4 mm. Fig. 7a shows variations of $\dot{m}\mu l$ versus $\rho A \Delta P$ for the four wick structures. The slope of the curves represents the wick permeability. As evident, the HW4-coarse and HW4-fine homogenous wick structures have the highest (i.e., 0.28 mm²) and the lowest (i.e., 0.12 mm²) permeability values, respectively. The GW4 gradient wick structure with a permeability of 0.24 mm² has a permeability higher than the HW4-medium but lower than the HW4-coarse. However, the permeability is not the only factor that should be considered. To delay the capillary limit, the combination of the permeability and capillary pressure values should be improved. Fig. 7b shows measured permeability versus estimated capillary pressure for the four wick structures. The capillary pressure was estimated from the Young-Laplace equation as follows:

$$P_c = \frac{2\sigma \cos\theta}{r_p} \quad (20)$$

where P_c is the capillary pressure, σ is the surface tension of the liquid, θ the contact angle between the solid and liquid phases, and r_p is the pore size. Considering a contact angle of 60°, capillary pressures of homogenous and gradient wick structures were estimated. For the GW4 gradient wick structure, the capillary pressure is governed by the pore size of the finest mesh layers (i.e., 228.6 μm). As evident, there is a strong dependency between the permeability and capillary pressure of the homogenous wick structures. The HW4-coarse homogenous wick structure demonstrates a high permeability but a low capillary pressure. The reverse is correct for the HW4-fine homogenous wick structure. However, the gradient wick structures could partially decouple the permeability and capillary pressure dependency. As shown in Fig. 7b, the GW4 gradient wick structure offers high capillary pressure and a relatively high permeability value compared with those of the homogenous wick structures. Therefore, it is expected that the GW4 gradient wick structure could offer a higher capillary limit and thus a higher flow boiling performance compared with a homogenous wick structure. This conclusion will be evaluated in the next section.

4.2. Role of channel wickability in flow boiling

To understand the role of channel wickability in the forced convection boiling process, experimental test results of the GW4 gradient wick channels were compared with those of the HW4-medium homogenous wick channels. Two additional heat sinks with a solid fin channel (SF4) and a plain copper substrate (PO) were also considered for comparison. The SF4 heat sink has similar geometrical dimensions (i.e., length, height, width, and spacing) as the

Table 3
Range and uncertainty of main parameters.

Parameter (measurement device) [unit]	Range	Nominal	Accuracy
Voltage (source meter, Keithley 2100) [V]	1-750	80	±(0.08% of reading + 0.04% of range)
Current (Fluke 323) [A]	0-400	8	± 2%
Mass flow rate (Omega-FT044-15-ST-VN) [g/sec]	2-18	8	±2%
Net fluid cross-sectional area [mm ²]	29-32	30	0.02 [mm ²]
Mass flux [kg/m ² -s]	140-340	240	±3%
Pressure difference (Omega-PX26-005DV) [psi]	0 to 5	1	±1%
T-type thermocouple (Omega-TMTSS) [°C]	60-315	180	±1 [°C]
K-type thermocouple (Omega-KMTSS) [°C]	100-800	400	±2 [°C]
Physical distance (digital caliper) [mm]	2-5	4	0.02 [mm]
Projected heat transfer area [mm ²]	-	100	0.03 [mm ²]
Permeability [mm ²]	0.1-0.3	0.2	± 3-7%
Heat flux [W/cm ²]	80-900	400	± 8-12%
Heat transfer coefficient [kW/m ² -K]	100-1050	250	± 16-32%

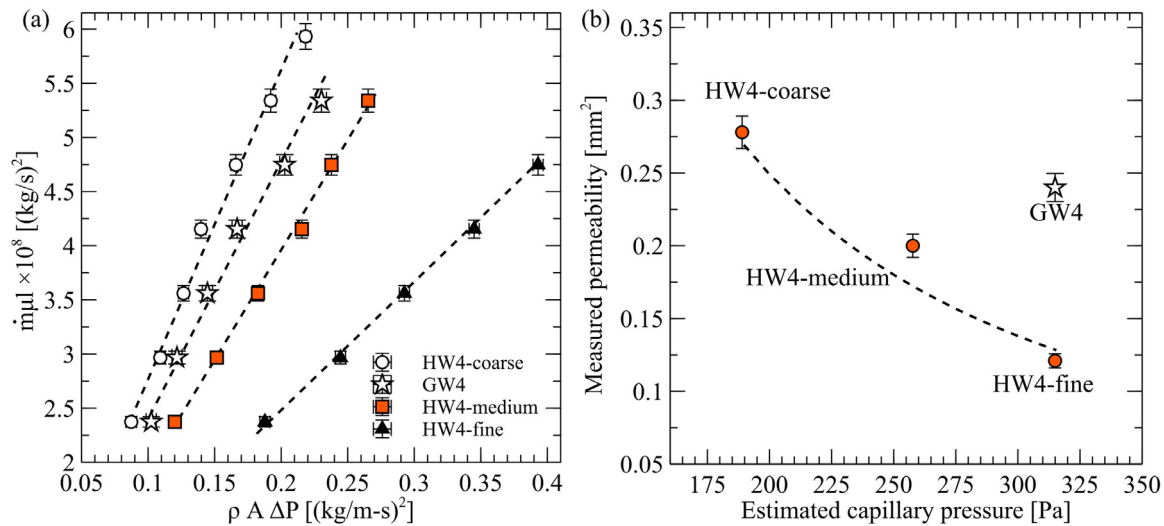


Fig. 7. (a) Variations of $\dot{m}\mu$ as a function of $\rho A \Delta P$, and (b) measured permeability versus estimated capillary pressure for homogenous and gradient wick structures.

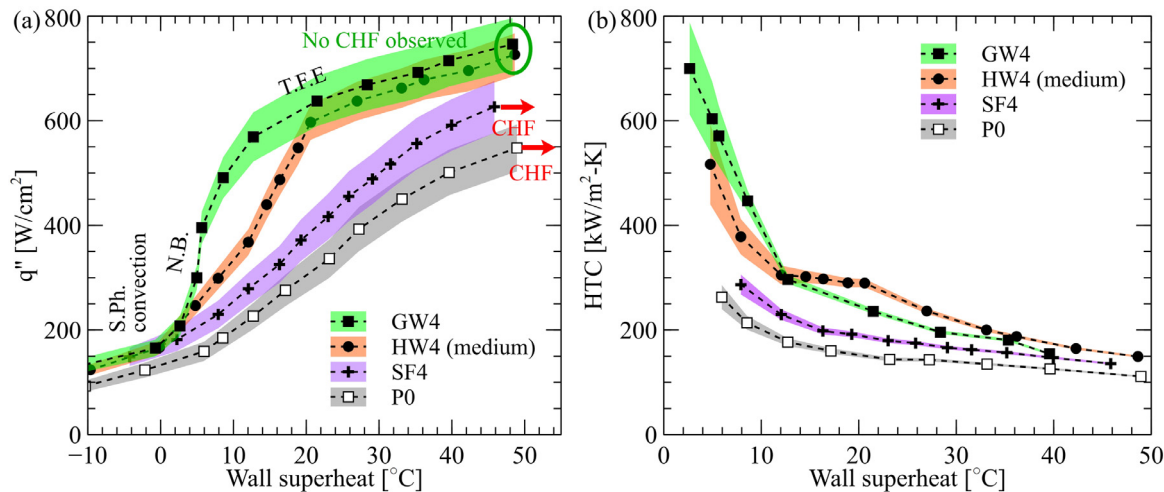


Fig. 8. (a) Heat fluxes and (b) heat transfer coefficients of the GW4 gradient wick channels, the HW4-medium homogenous wick channels, the SF4 solid fin channels, and the PO bare copper substrate at different wall superheats. S.Ph., N.B., and T.F.E. stand for single phase, nucleate boiling, and thin film evaporation, respectively.

GW4 and HW4-medium wick heat sinks. Fig. 8 shows flow boiling curves and HTC of these four surfaces at different wall superheats and a fixed mass flux of 240 kg/m²-s. The heat flux was calculated considering a total projected footprint area of 1 cm². At low wall superheats, heat transfer is dominated by the single-phase forced convection mode. In this regime, surface heat fluxes of all samples are almost identical with a slight increase in observed heat

flux values with wall superheats, typical of single-phase convection heat transfer.

Measured heat fluxes of all test surfaces rapidly increase once the nucleate flow boiling process initiates at a wall superheat range of approximately 5-8°C. As shown, the surface heat flux and HTC (i.e., the slope of the heat transfer curve) of the GW4 gradient wick channels are meaningfully higher than those of the HW4-

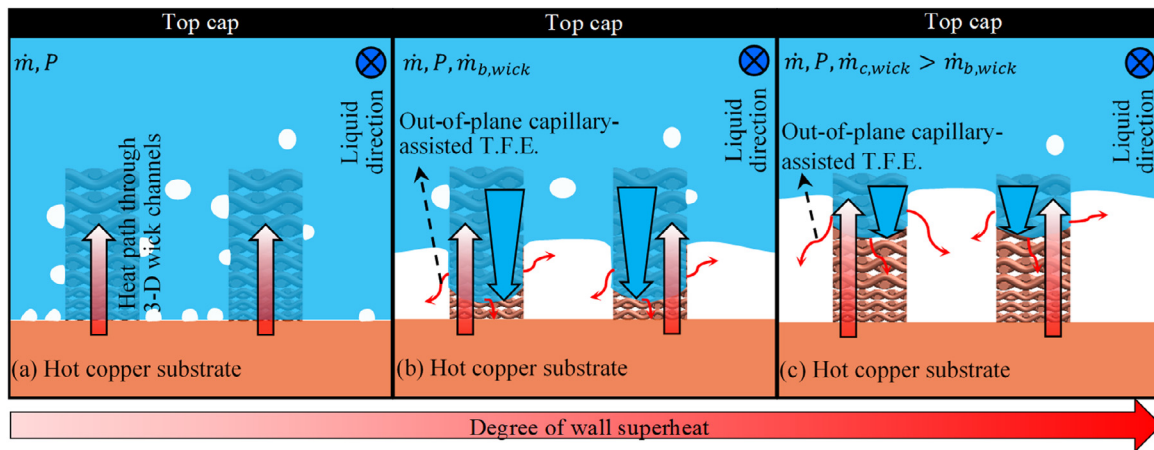


Fig. 9. Possible schematics of the transient liquid-vapor interface present in the gradient wick channel topology at different wall superheats: (a) low, (b) medium, and (c) high wall superheats.

medium homogenous wick channels. This can be attributed to the improved capillary limit of the GW4 gradient wick structure compared with that of the HW4-medium wick structure. A gradient wick channel could partially decouple the permeability and capillary pressure, thereby improving the capillary limit and thus surface heat flux and HTC at a given wall superheat. This is consistent with the conclusion drawn in Subsection 4.1. Additionally, both the GW4 and HW4-medium wick structures outperform the SF4 and P0 heat sinks. This is because of unique thermo-fluidic features offered by the 3D wick channels including a higher number of active nucleation sites, additional surface areas for phase change heat transfer, and improved wickability through tortuous micro-inflow passages.

It can be seen that slopes of the heat flux curves associated with the GW4, HW4, and SF4 boiling surfaces alter at a heat flux close to the CHF limit of the bare copper substrate (i.e., surface heat flux of approximately 550 W/cm^2). The heat sink with solid channels experiences the CHF limit soon after its slope changes. The CHF limit of the solid channel surface is slightly higher than that of the bare copper substrate mainly due to its added surface area and active nucleation sites through the solid channel walls. However, interestingly, no CHF limit was observed on both GW4 and HW4-medium wick channels even at wall superheats as high as $65 \text{ }^\circ\text{C}$. This can be attributed to the out-of-plane capillary-assisted T.F.E. (thin-film evaporation) mechanism enabled by the through-vapor thermal-wick bridges facilitating both the heat dissipation paths and the liquid delivery routes. Here, the cooler far-field liquid is wicked into the gradient wick channels (cf. Fig. 9), thereby resulting in a highly-efficient thin film evaporation process through liquid-vapor interfaces formed within and around the wick channels. The flow boiling process in this regime is affected by the capillary-assisted thin-film evaporation mechanism controlled by the liquid mass flow rate. The thin-film evaporation process is activated through out-of-plane wicking action. The slope of the heat flux curve representing the efficiency of the T.F.E mechanism can be improved if one optimizes the wick channel topology and far-field liquid pressure. In the T.F.E. regime, the flow boiling heat fluxes of both GW4 and HW4-medium wick channels are almost identical. This could be attributed to the position of the liquid-vapor interfaces, which might be predominantly established away from the bottom hot surface where the GW4 gradient wick channel employs medium and/or coarse pore size meshes (cf. Fig. 9c). Under this circumstance, the capillary pressure of both GW4 and HW4-medium wick structure is governed by the medium pore size mesh, thereby leading to similar flow boiling heat fluxes as indicated in Fig. 8a. It should be noted that, at a wall superheat

of $65 \text{ }^\circ\text{C}$, the temperature of the heating block exceeded $800 \text{ }^\circ\text{C}$ which is the maximum safe operating temperature of the cartridge heaters employed. Therefore, the flow boiling experiments typically stopped at a wall superheat of about $55 \text{ }^\circ\text{C}$.

4.3. Role of convection in flow boiling on gradient wick channel surfaces

Fig. 10a and b show flow boiling experimental test results of the GW4 gradient wick channel topology and the P0 plain copper substrate at different mass fluxes. As shown, the effect of mass flow rate (i.e., convective flow) on flow boiling on the bare copper substrate is indistinguishable. Flow boiling process on the gradient wick channel topology, however, demonstrates a strong liquid mass flux dependency. Here, a combination of convective boiling and wickability effects (i.e., a higher combination of permeability and capillary pressure) boosts the heat dissipation rate. Additionally, the CHF limit was not observed on the gradient wick channel surface in the mass flux and wall superheat range investigated.

The effect of augmented wickability at higher flow rates could be explained considering far-field average liquid pressure which increases at higher liquid mass flow rates as shown in Fig. 11. This consequently leads to a higher effective capillary pressure for the wicking action and thus enhanced wicked micro-inflows through the gradient wick channels (i.e., \dot{m}_{wick}) as schematically illustrated in Fig. 12. As a result, the heat flux fraction associated with the wicked micro-inflows (i.e., $q'' \propto \dot{m}_{wick} h_{fg}$) is substantially improved at higher mass fluxes as clearly indicated in Fig. 10. Additionally, Fig. 11 shows pressure drop values of the GW4 gradient wick heat sink at wall superheats of 20 and $30 \text{ }^\circ\text{C}$ for different mass fluxes. As evident, at higher heat fluxes, pressure drop values increase with mass flow rates due to augmented friction and acceleration pressure losses.

4.4. Role of out-of-plane wicking length scale in the flow boiling process

In the proposed gradient wick topology, the wicking length scale is considered as the height of a wick channel bridging unstable vapor cushion layers formed at high wall superheats through the capillary-assisted thin-film evaporation mechanism. Generally, it can be perceived that a heat sink with a longer out-of-plane wicking length scale could bridge a thicker vapor film, thereby potentially leading to higher heat flux values. To verify this hypothesis, another heat sink topology with a wick channel height of

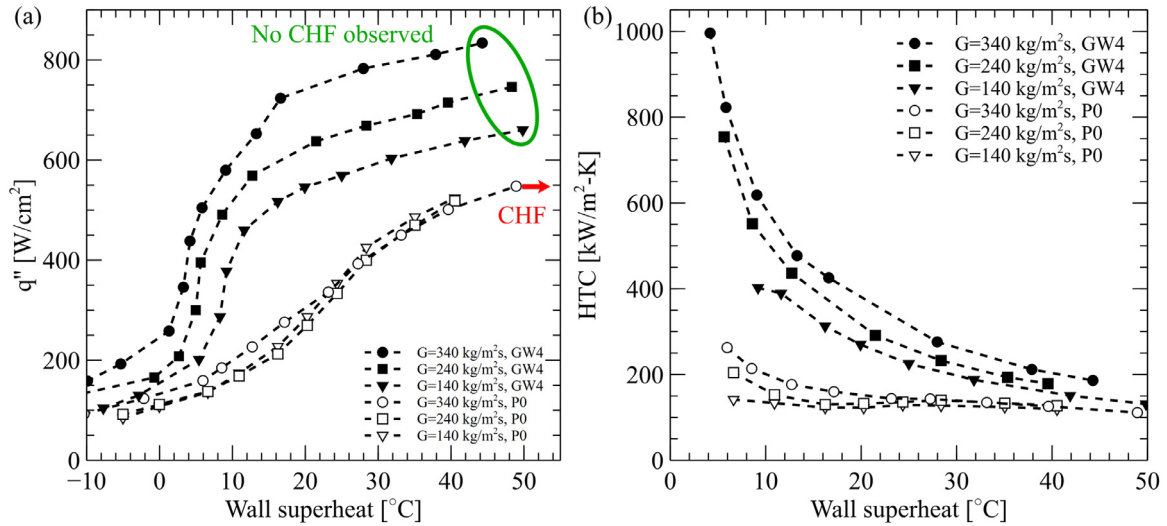


Fig. 10. (a) Heat fluxes and (b) heat transfer coefficients of the GW4 gradient wick channel topology and P0 plain substrate at different wall superheats and mass fluxes. Red arrow indicates CHF limit.

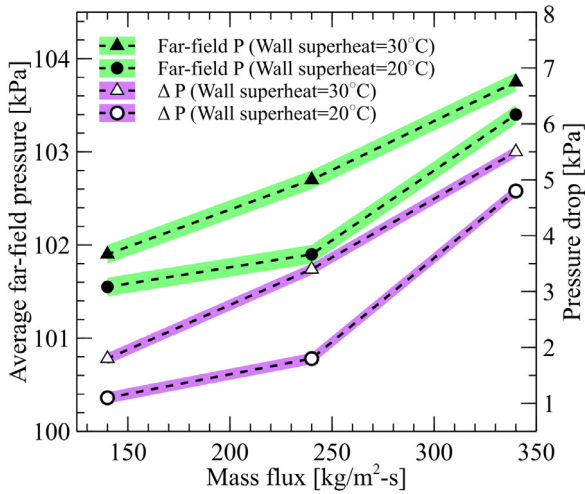


Fig. 11. Average far-field pressure and pressure drop of the GW4 heat sink at different wall superheats.

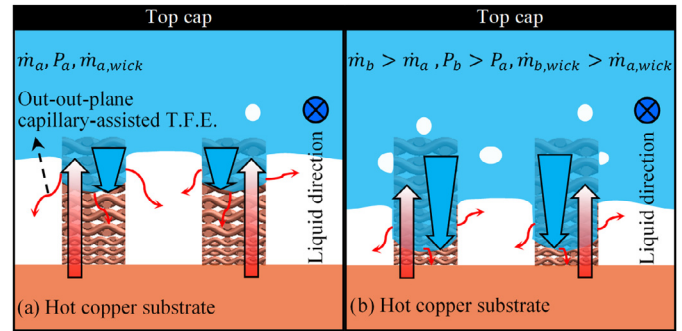


Fig. 12. Possible schematics of the transient liquid-vapor interface of the gradient wick channel topology at a (a) low, and (b) high mass flux value.

2.5 mm (GW2.5) is fabricated and tested. Fig. 13 shows flow boiling curves and HTCs of the gradient wick channel heat sinks with 2.5 and 4 mm heights, and the P0 plain copper substrate at different wall superheats and mass fluxes. As shown, the GW2.5 heat

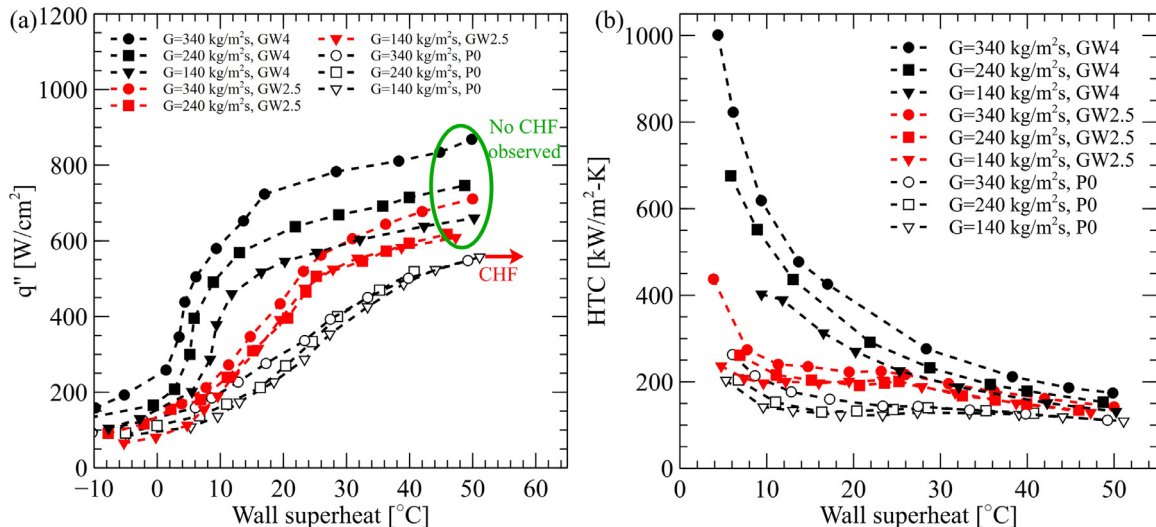


Fig. 13. (a) Heat fluxes and (b) heat transfer coefficients of the GW4 and GW2.5 gradient wick channel heat sinks at different wall superheats and flow rates. Red arrows indicate CHF limits for each experiment. (For interpretation of the references to color in this figure legend, the reader is referred to the web version of this article.)

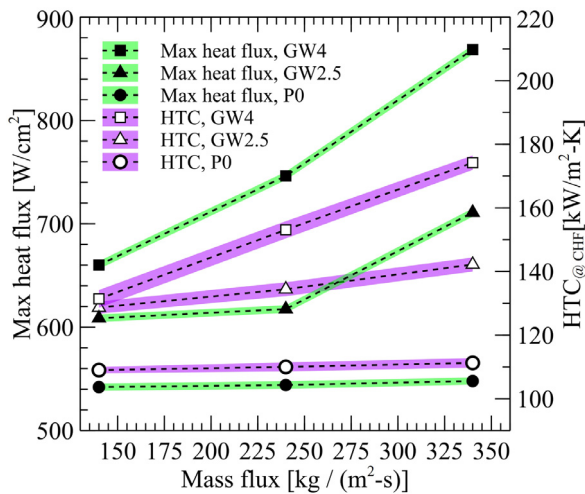


Fig. 14. Heat fluxes and heat transfer coefficients of various heat sinks explored in the present study.

sink device demonstrates a thermal performance behavior with observed heat transfer mechanisms similar to those of the GW4 heat sink. However, at a given mass flux, the GW2.5 heat sink exhibits a lower heat flux value than the GW4 heat sink due to a shorter out-of-plane wicking length scale available to bridge the transient vapor gaps formed at high wall superheats. It should be noted that a gradient wick channel with a higher height than the GW4 gradient heat sink might not necessarily increase the heat flux significantly. This is attributed to the thermo-hydraulic status of the cooler far-field liquid phase, which reaches the saturation temperature and pressure condition. Therefore, a gradient wick channel with a substantially higher height might only travel deeper into the cooler liquid phase without meaningfully improving flow boiling thermal performance. In this study, a gradient wick structure with a height exceeding that of the GW4 heat sink was not tested mainly due to fabrication limitations associated with diffusion bonding and machining of thicker wick structures.

Fig. 14 shows heat flux and corresponding HTC values measured on various examined heat sinks at a wall superheat of 50 °C and different mass fluxes. While the flow boiling performance of the plain copper substrate is almost insensitive to convective effects in the range investigated, the proposed gradient wick channel topology effectively leverages mass flow rate through the capillary-assisted thin-film evaporation mechanism. Here, effective capillary pressure available for micro-inflows wicked into the gradient channels increases at higher mass flow rates, thereby further boosting the heat transfer rate. Additionally, the gradient wick channels outperform the homogenous wick channels due to an improved wickability action and capillary limit. Furthermore, it was observed that heat sinks with longer available wicking lengths can bridge thicker vapor films, thereby leading to higher heat fluxes at high wall superheats.

4.5. Flow boiling performance comparison with the open literature

Fig. 15 compares the maximum heat flux and HTC of the proposed gradient wick channel heat sink with several selected studies [1,46–50] from the open literature for the flow boiling process. The corresponding mass fluxes and heat sink topologies of selected studies are mentioned. As shown, the heat sink topologies of the selected studies include a microchannel with a tapered gap manifold [48], two microchannel heat sinks employing micro-pillars [49,50], a microchannel heat sink with a roughened surface [46], a microchannel heat sink with reentrant cavities [47], and

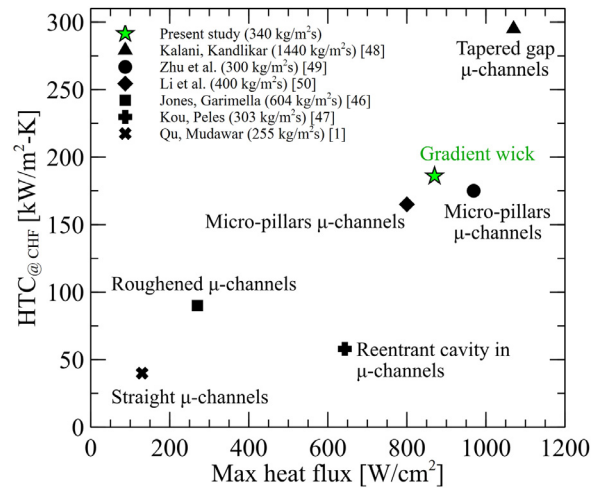


Fig. 15. A comparison between flow boiling performance of the proposed gradient wick channels and several selected studies.

a straight flow microchannel heat sink [1]. As shown, at a mass flux of 340 kg/m²-s, the proposed gradient wick channel heat sink demonstrates moderately high heat flux and HTC values due to its improved capillary limit and unique thermo-fluidic features.

5. Conclusion

In this study, a new heat sink architecture utilizing copper-based gradient wick channels was proposed to both enhance HTC and delay the CHF limit of the flow boiling process. Permeability tests showed that the gradient wick structures offer a better combination of permeability and capillary pressure, thereby potentially delaying the capillary limit and improving thermal performance metrics. Phase-change experiments indeed confirmed that the gradient wick channel topology outperforms the homogenous wick channels, solid fin channels, and plain copper surfaces for the flow boiling process. The proposed gradient wick channel heat sink demonstrated a strong liquid mass flux dependency in the flow rate range explored. This can be attributed to a combination of convective boiling and amplified wickability effects improving the heat dissipation rate. Beyond offering a higher number of active nucleation sites and additional surface area for phase change heat transfer, the proposed heat sink architecture exhibits augmented out-of-plane wickability through its gradient wick topology. At higher mass flow rates, far-field average liquid pressure available for capillary wicking action increases. This consequently boosts wicked micro-inflows toward the bottom hot surface, thereby resulting in a highly-efficient thin film evaporation process and enhanced heat transfer rate. In fact, the CHF limit was not observed on the gradient wick channel surfaces in the mass flux and wall superheat range studied. The experimental results indicated a maximum flow boiling CHF limit of 870 W/cm² with a 4-mm-in-height gradient wick channel heat sink. This is a 60% enhancement in flow boiling heat flux compared with that of a plain copper surface. Moreover, a maximum HTC of 1000 kW/m²-K at a wall superheat of 3 °C was observed. Experiments conducted here confirmed the promise of the proposed gradient wick channel heat sink architecture for future high-heat-flux applications such as high-power electronics.

Declaration of Competing Interest

The authors declare that they have no known competing financial interests or personal relationships that could have appeared to influence the work reported in this paper.

CRediT authorship contribution statement

Masoud Ahmadi: Investigation, Formal analysis, Data curation, Visualization, Writing - original draft. **Sajjad Bigham:** Conceptualization, Supervision, Methodology, Visualization, Funding acquisition, Writing - original draft, Writing - review & editing.

References

- W. Qu, I. Mudawar, Flow boiling heat transfer in two-phase micro-channel heat sinks—II. Annular two-phase flow model, *Int. J. Heat Mass Transf.* 46 (2003) 2773–2784, doi:10.1016/S0017-9310(03)00042-5.
- W. Yu, D.M.M. France, M.W.W. Wambsganss, J.R.R. Hull, Two-phase pressure drop, boiling heat transfer, and critical heat flux to water in a small-diameter horizontal tube, *Int. J. Multiph. Flow.* 28 (2002) 927–941, doi:10.1016/S0301-9322(02)00019-8.
- G.R. Warriar, V.K. Dhir, L.A. Momoda, Heat transfer and pressure drop in narrow rectangular channels, *Exp. Therm. Fluid Sci.* 26 (2002) 53–64, doi:10.1016/S0894-1777(02)00107-3.
- W. Qu, I. Mudawar, Measurement and correlation of critical heat flux in two-phase micro-channel heat sinks, *Int. J. Heat Mass Transf.* 47 (2004) 2045–2059, doi:10.1016/j.ijheatmasstransfer.2003.12.006.
- Z. Lu, T.R. Salamon, S. Narayanan, K.R. Bagnall, D.F. Hanks, D.S. Antao, B. Barabadi, J. Sircar, M.E. Simon, E.N. Wang, Design and modeling of membrane-based evaporative cooling devices for thermal management of high heat fluxes, *IEEE Trans. Compon., Packag. Manuf. Technol.* 6 (2016) 1056–1065, doi:10.1109/TCPM.2016.2576998.
- R.L. Webb, N.-H. Kim, *Principle of enhanced heat transfer*, Taylor & Francis Group, 1994.
- M.B. Bowers, I. Mudawar, High flux boiling in low flow rate, low pressure drop mini-channel and micro-channel heat sinks, *Int. J. Heat Mass Transf.* 37 (1994) 321–332, doi:10.1016/0017-9310(94)90103-1.
- A.P. Ornatkii, L.S. Vinyarskii, Heat transfer crisis in a forced flow of underheated water in small-bore tubes, *Teplofiz. Vysok. Temp.* 3 (1965) 441–451.
- K.P. Bloschok, A. Bar-Cohen, Advanced thermal management technologies for defense electronics, in: *Proc. SPIE Vol. 8405*, 2012 84050I-84050I-12, doi:10.1117/12.924349.
- A. Bar-Cohen, K. Matin, N. Jankowski, D. Sharar, Two-phase thermal ground planes: technology development and parametric results, *J. Electron. Packag.* 137 (2014) 10801, doi:10.1115/1.4028890.
- J.Y. Lee, M.-H. Kim, M. Kaviani, S.Y. Son, Bubble nucleation in microchannel flow boiling using single artificial cavity, *Int. J. Heat Mass Transf.* 54 (2011) 5139–5148, doi:10.1016/j.ijheatmasstransfer.2011.08.042.
- C.M. Patil, S.G. Kandlikar, Pool boiling enhancement through microporous coatings selectively electrodeposited on fin tops of open microchannels, *Int. J. Heat Mass Transf.* 79 (2014) 816–828, doi:10.1016/j.ijheatmasstransfer.2014.08.063.
- R. Chen, M.-C. Lu, V. Srinivasan, Z. Wang, H.H. Cho, A. Majumdar, Nanowires for enhanced boiling heat transfer, *Nano Lett.* 9 (2009) 548–553, doi:10.1021/nl8026857.
- C. Li, Z. Wang, P.-I. Wang, Y. Peles, N. Koratkar, G.P. Peterson, Nanostructured copper interfaces for enhanced boiling, *Small* 4 (2008) 1084–1088, doi:10.1002/sml.200700991.
- T. Liu, S. Lingamneni, J. Palko, M. Asheghi, K.E. Goodson, Optimization of hybrid wick structures for extreme spreading in high performance vapor chambers, in: *2016 15th IEEE Intersoc. Conf. Therm. Thermomechanical Phenom. Electron. Syst.*, 2016, pp. 30–36, doi:10.1109/ITHERM.2016.7517524.
- J.W. Palko, H. Lee, D.D. Agonafer, C. Zhang, K.W. Jung, J. Moss, J.D. Wilbur, T.J. Dusseault, M.T. Barako, F. Houshmand, G. Rong, T. Maitra, C. Gorle, Y. Won, D. Rockosi, I. Mykyta, D. Resler, D. Altman, M. Asheghi, J.G. Santiago, K.E. Goodson, High heat flux two-phase cooling of electronics with integrated diamond/porous copper heat sinks and microfluidic coolant supply, in: *2016 15th IEEE Intersoc. Conf. Therm. Thermomechanical Phenom. Electron. Syst.*, 2016, pp. 1511–1517, doi:10.1109/ITHERM.2016.7517728.
- F. Yang, X. Dai, Y. Peles, P. Cheng, C. Li, Can multiple flow boiling regimes be reduced into a single one in microchannels? *Appl. Phys. Lett.* 103 (2013) 043122, doi:10.1063/1.4816594.
- Z.Y. Y.W.L. S.G. Kandlikar, Fabrication of nanowires on orthogonal surfaces of microchannels and their effect on pool boiling, *J. Micromech. Microeng.* 22 (2012) 115005.
- D. Li, G.S. Wu, W. Wang, Y.D. Wang, D. Liu, D.C. Zhang, Y.F. Chen, G.P. Peterson, R. Yang, Enhancing flow boiling heat transfer in microchannels for thermal management with monolithically-integrated silicon nanowires, *Nano Lett.* 12 (2012) 3385–3390, doi:10.1021/nl300049f.
- K.-H. Chu, Y. Soo Jeong, R. Enright, C.R. Buie, E.N. Wang, Hierarchically structured surfaces for boiling critical heat flux enhancement, *Appl. Phys. Lett.* 102 (2013) 151602, doi:10.1063/1.4801811.
- K.-H. Chu, R. Enright, E.N. Wang, Structured surfaces for enhanced pool boiling heat transfer, *Appl. Phys. Lett.* 100 (2012) 241603, doi:10.1063/1.4724190.
- H. O'Hanley, C. Coyle, J. Buongiorno, T. McKrell, L.-W. Hu, M. Rubner, R. Cohen, Separate effects of surface roughness, wettability, and porosity on the boiling critical heat flux, *Appl. Phys. Lett.* 103 (2013) 024102, doi:10.1063/1.4813450.
- S. Ravi, R. Dharmarajan, S. Moghaddam, Physics of fluid transport in hybrid biporous capillary wicking microstructures, *Langmuir* 32 (2016) 8289–8297, doi:10.1021/acs.langmuir.6b01611.
- J.J. Wei, H. Honda, Effects of fin geometry on boiling heat transfer from silicon chips with micro-pin-fins immersed in FC-72, *Int. J. Heat Mass Transf.* 46 (2003) 4059–4070, doi:10.1016/S0017-9310(03)00226-6.
- J.M. Kim, T. Kim, J. Kim, M.H. Kim, H.S. Ahn, Effect of a graphene oxide coating layer on critical heat flux enhancement under pool boiling, *Int. J. Heat Mass Transf.* 77 (2014) 919–927, doi:10.1016/j.ijheatmasstransfer.2014.06.017.
- H.S. Ahn, H.J. Jo, S.H. Kang, M.H. Kim, Effect of liquid spreading due to nano/microstructures on the critical heat flux during pool boiling, *Appl. Phys. Lett.* 98 (2011) 071908, doi:10.1063/1.3555430.
- H. Seo, J.H. Chu, S.-Y. Kwon, I.C. Bang, Pool boiling CHF of reduced graphene oxide, graphene, and SiC-coated surfaces under highly wettable FC-72, *Int. J. Heat Mass Transf.* 82 (2015) 490–502, doi:10.1016/j.ijheatmasstransfer.2014.11.019.
- S. Bigham, S. Moghaddam, Physics of the microchannel flow boiling process and comparison with the existing theories, *J. Heat Transf.* 139 (2017) 111503–111510.
- S. Bigham, S. Moghaddam, Role of bubble growth dynamics on microscale heat transfer events in microchannel flow boiling process, *Appl. Phys. Lett.* 107 (2015) 244103.
- S. Bigham, S. Moghaddam, Microscale study of mechanisms of heat transfer during flow boiling in a microchannel, *Int. J. Heat Mass Transf.* 88 (2015) 111–121.
- E. Forrest, E. Williamson, J. Buongiorno, L.-W. Hu, M. Rubner, R. Cohen, Augmentation of nucleate boiling heat transfer and critical heat flux using nanoparticle thin-film coatings, *Int. J. Heat Mass Transf.* 53 (2010) 58–67, doi:10.1016/j.ijheatmasstransfer.2009.10.008.
- M.M. Rahman, E. Ölçeroğlu, M. McCarthy, Role of wickability on the critical heat flux of structured superhydrophilic surfaces, *Langmuir* 30 (2014) 11225–11234.
- S.G. Liter, M. Kaviani, Pool-boiling CHF enhancement by modulated porous-layer coating: theory and experiment, *Int. J. Heat Mass Transf.* 44 (2001) 4287–4311, doi:10.1016/S0017-9310(01)00084-9.
- A. Jaikumar, S.G. Kandlikar, Pool boiling enhancement through bubble induced convective liquid flow in feeder microchannels, *Appl. Phys. Lett.* 108 (2016) 41604, doi:10.1063/1.4941032.
- M.M. Rahman, J. Pollack, M. McCarthy, Increasing boiling heat transfer using low conductivity materials, *Sci. Rep.* 5 (2015) 13145, doi:10.1038/srep13145.
- M.M. Rahman, M. McCarthy, Boiling enhancement on nanostructured surfaces with engineered variations in wettability and thermal conductivity, *Heat Transf. Eng.* 38 (2017) 1285–1295, doi:10.1080/01457632.2016.1242961.
- S. Zhang, X. Jiang, Y. Li, G. Chen, Y. Sun, Y. Tang, C. Pan, Extraordinary boiling enhancement through micro-chimney effects in gradient porous micromeshes for high-power applications, *Energy Convers. Manag.* 209 (2020) 112665, doi:10.1016/j.enconman.2020.112665.
- A. Kalani, S.G. Kandlikar, Experimental investigation of flow boiling performance of open microchannels with uniform and tapered manifolds (OMM), Vol. 2 *Heat Transf. Enhanc. Pract. Appl. Heat Mass Transf. Fire Combust. Heat Transf. Multiph. Syst. Heat Mass Transf. Biotechnol.*, ASME, 2013 V002T07A018, doi:10.1115/HT2013-17441.
- S.G. Kandlikar, T. Widger, A. Kalani, V. Mejia, Enhanced flow boiling over open microchannels with uniform and tapered gap manifolds, *J. Heat Transf.* 135 (2013) 061401, doi:10.1115/1.4023574.
- M.P. David, J. Miler, J.E. Steinbrenner, Y. Yang, M. Touzelbaev, K.E. Goodson, Hydraulic and thermal characteristics of a vapor venting two-phase microchannel heat exchanger, *Int. J. Heat Mass Transf.* 54 (2011) 5504–5516, doi:10.1016/j.ijheatmasstransfer.2011.07.040.
- A. Fazeli, S. Bigham, S. Moghaddam, Microscale layering of liquid and vapor phases within microstructures for a new generation two-phase heat sink, *Int. J. Heat Mass Transf.* 95 (2016) 368–378, doi:10.1016/j.ijheatmasstransfer.2015.12.005.
- A. Fazeli, M. Mortazavi, S. Moghaddam, Hierarchical biphilic micro/nanostructures for a new generation phase-change heat sink, *Appl. Therm. Eng.* 78 (2015) 380–386, doi:10.1016/j.applthermaleng.2014.12.073.
- S. Bigham, A. Fazeli, S. Moghaddam, Physics of microstructures enhancement of thin film evaporation heat transfer in microchannels flow boiling, *Sci. Rep.* 7 (2017) 44745, doi:10.1038/srep44745.
- N.S. Dhillon, J. Buongiorno, K.K. Varanasi, Critical heat flux maxima during boiling crisis on textured surfaces, *Nat. Commun.* 6 (2015) 8247.
- D.J. Huang, T.S. Leu, Fabrication of high wettability gradient on copper substrate, *Appl. Surf. Sci.* 280 (2013) 25–32, doi:10.1016/j.apsusc.2013.04.065.
- B.J. Jones, S.V. Garimella, Surface roughness effects on flow boiling in microchannels, *J. Therm. Sci. Eng. Appl.* 1 (2009) 1–9, doi:10.1115/1.4001804.
- C.-J. Kuo, Y. Peles, Local measurement of flow boiling in structured surface microchannels, *Int. J. Heat Mass Transf.* 50 (2007) 4513–4526, doi:10.1016/j.ijheatmasstransfer.2007.03.047.
- A. Kalani, S.G. Kandlikar, Combining liquid inertia with pressure recovery from bubble expansion for enhanced flow boiling, *Appl. Phys. Lett.* 107 (2015) 1–5, doi:10.1063/1.4935211.
- Y. Zhu, D.S. Antao, K.H. Chu, S. Chen, T.J. Hendricks, T. Zhang, E.N. Wang, Surface structure enhanced microchannel flow boiling, *J. Heat Transf.* 138 (2016) 1–13, doi:10.1115/1.4033497.
- W. Li, Z. Wang, F. Yang, T. Alam, M. Jiang, X. Qu, F. Kong, A.S. Khan, M. Liu, M. Alwazzan, Y. Tong, C. Li, Supercapillary architecture-activated two-phase boundary layer structures for highly stable and efficient flow boiling heat transfer, *Adv. Mater.* (2020) 32, doi:10.1002/adma.201905117.